Journal of Materials Chemistry A

Effects of a solid electrolyte coating on the discharge kinetics of a LiCoO2 electrode: Mechanism and potential applications

Journal:	*Journal of Materials Chemistry A*
Manuscript ID	TA-ART-06-2020-005656.R2
Article Type:	Paper
Date Submitted by the Author:	14-Sep-2020
Complete List of Authors:	Charles-Blin, Youn ; Shinshu University Faculty of Engineering, Department of Materials Chemistry Nemoto, Kazune; Shinshu University, Department of Materials Chemistry Zettsu, Nobuyuki; Shinshu University Faculty of Engineering, Department of Materials Chemistry; Shinshu University, Research Initiative for Supra-Materials Teshima, Katsuya; Shinshu University Faculty of Engineering, Department of Materials Chemistry; Shinshu University, Research Initiative for Supra-Materials

ARTICLE

Effects of a solid electrolyte coating on the discharge kinetics of a $LiCoO_2$ electrode: Mechanism and potential applications

Received 00th January 20xx,
Accepted 00th January 20xx

DOI: 10.1039/x0xx00000x

Youn Charles-Blin,[a] Kazune Nemoto,[a] Nobuyuki Zettsu,[a,b,*] and Katsuya Teshima,[a,b,*]

The application of a Li^+-conductive amorphous $Li_2B_4O_7$ coating to a $LiCoO_2$ electrode enhanced its discharge kinetics by increasing the local concentration of Li^+ at the surface of $LiCoO_2$ particles. The origin of internal resistance in Li^+ intercalation steps was elucidated by electrochemical impedance spectroscopy (EIS)-based characterization of discharge kinetics for states of charges of 0, 50, and 100%, while the activation energies of intercalation steps were determined from EIS data collected at different temperatures (−10, 0, 20, and 40 °C). The activation energy of Li^+ desolvation was smaller than that previously reported for bare $LiCoO_2$ particles, which suggested that the significant changes in kinetics associated with polarization mitigation were due to Li^+ exchange reaction (Li^+ adsorption and diffusion processes) on the surface of $LiCoO_2$ particles. Finally, C-rate capability tests performed at −10 °C revealed that the capacity retention of the electrode comprising $Li_2B_4O_7$-coated $LiCoO_2$ particles exceeded that of the electrode comprising bare $LiCoO_2$ particles (45% vs. 18%, respectively).

Introduction

The operation of lithium-ion batteries (LIBs) involves the sequential or simultaneous occurrence of a multitude of such reactions complicates the investigation of their mechanisms, e.g., although the degradation of liquid electrolytes during battery cycling in a certain electrochemical potential window is known to afford a solid electrolyte interphase (SEI) and cathode electrolyte interphase (CEI),[1] the interactions of liquid electrolytes with electrode surfaces at the atomic/molecular level remain poorly understood. Moreover, even though LIBs have found numerous applications, the demand for higher power densities necessitates the design of more efficient LIBs that relies on the enhancement of Li^+ intercalation kinetics to accelerate charge and discharge reactions. The identification of the intercalation rate–controlling step is therefore of paramount importance for this enhancement. For LIBs, charge transfer involves the steps of Li^+ diffusion within the electrolyte, the subsequent desolvation, adsorption, and diffusion of Li^+ through the CEI and on the active material surface, and Li^+ insertion into the active material. Abe *et al.*[2,3] reported that intercalation kinetics is largely determined by Li^+ desolvation rather than by Li^+ diffusion through the CEI, further showing that the activation energy of desolvation was positively correlated with the interaction between lithium ion and solvent. These authors also studied Li^+ transfer at the ceramic-based solid electrolyte/liquid electrolyte interphase by electrochemical impedance spectroscopy (EIS), concluding that the overall reaction kinetics was determined by the activation energy of desolvation of the liquid electrolyte, as it exceeded that of the solid electrolyte. Jow *et al.*[4] identified the conditions under which charge transfer kinetics is controlled by the desolvation of Li^+ ions or their transport through the CEI. In particular, it was shown that at high temperatures, charge transfer may be limited by the diffusion of Li^+ through the active material bulk or through the CEI, whereas desolvation becomes the limiting factor in the case of an amorphous electrolyte interphase or a very thin CEI.

The need to improve the reaction kinetics determined by these rate-controlling steps as well as surface reactivity has inspired investigations of the effects of local Li^+ concentration on LIB power density,[5,6,15,16,7–14] or as exemplified by works on the effects of coating the surface of $LiCoO_2$ (LCO) cathode materials with the $Li_2B_4O_7$ (LBO) glass electrolyte. Lithium borates and related compounds[17] exhibit moderate ionic conductivities (ca.10^{-7} S cm^{-1}) much smaller than those of other solid electrolytes such as crystalline $Li_{10}GeP_2S_{12}$ (1.2×10^{-2} S cm^{-1})[18] and crystalline argyrodite (Li_6PS_5Cl; 1.3×10^{-3} S cm^{-1}).[19] The ionic conductivity of amorphous compounds is relatively weakly affected by changes in composition during electetrochemical reactions, whereas that of crystalline solid electrolytes can change by several orders of magnitude.[20–22] Furthermore, the moderate ionic conductivity and the distinctively non-definite lattice constant of the amorphous phase prevent the increase in resistance due to the formation of a space charge layer at the interface and the lattice mismatch at the LBO-LCO interface. Finally, LBO coatings helps to increase the Li^+ density of cells, as solid electrolytes intrinsically feature a higher concentration of Li^+ than liquid ones.

---

[a] Department of Material Chemistry, Shinshu University, 4-17-1 Wakasato, Nagano, 380-8553 Japan
[b] Research Institute of Supra Materials, Shinshu University, 4-17-1 Wakasato, Nagano, 380-8553 Japan
*Corresponding Authors. zettsu@shinshu-u.c.jp, teshima@shinshu-u.ac.jp

Electronic Supplementary Information (ESI) available: Additional characterizations of electrode materials. See DOI: 10.1039/x0xx00000x

Herein, we coated LCO particles with amorphous $Li_2B_4O_7$ layers of variable thickness and investigated the chemical nature and morphology of these coatings as well as their influence on the C-rate capability of LCO electrodes at room temperature and −10 °C. The activation energies of Li^+ intercalation steps were calculated based on the results of EIS measurements performed at various states of charge (SOCs) and temperatures.

Experimental

Deposition of LBO coatings

LCO (99.99%) was provided by Nippon Chemical Industry Ltd., Japan. LBO was prepared from $LiOH \cdot H_2O$ (99.8%, Wako Pure Chemical Industries Ltd., Japan), H_3BO_3 (99.5%, Wako Pure Chemical Industries Ltd., Japan), and polyvinylpyrrolidone (PVP; Merck, Germany). A 100-ml disposable plastic pot containing ultra-pure water (20 ml) was charged with $LiOH \cdot H_2O$, H_3BO_3, and PVP (dispersant), and the dispersion was stirred at 23 °C until a clear transparent solution was obtained. Three solutions with different precursor loadings were used to prepare LCO particles with variable LBO layer thickness. Aqueous precursor solutions (1.67 ml) were coated using three cycles of [3-min kneading + 30-s defoaming] (Awatori Rentarou, AR-100, Sinky Ltd., Japan), and the obtained mixtures were filtered under reduced pressure. The collected powders were vacuum-dried at room temperature for 4 h (Yamato Scientific, DP33), confirmed to contain no large aggregates by naked-eye inspection, and heated to 500 °C in an alumina crucible at 900 °C h^{-1} for 10 h using a furnace (FO100, Yamato Scientific Ltd., Japan). The surface area and volume of LCO particles were calculated assuming that these particles were spherical, and the mean particle size was obtained as 7.0 μm (SALD-7100nano, Shimadzu Ltd., Japan). The volume of the LBO solution required per LCO particle was estimated from the particle surface area and the desired coating thickness. Subsequently, LCO particle volume and density (5.0 g cm^{-3}) were used to calculate the number of LCO particles in a 5.0-g sample and thus estimate the required LBO volume. Finally, the masses of precursors in the LBO solution were calculated from LBO density (2.4 g cm^{-3}) and volume. For instance, to achieve an LBO layer thickness of 100 nm, 5.0 g of LCO particles, 1.259 g of $LiOH \cdot H_2O$, and 3.710 g of H_3BO_3 were dispersed in 20 ml of pure water. In the case of other LBO layer thicknesses, the amount of LCO was fixed, and only the quantities of other components were changed. For a 34-nm-thick LBO layer, 0.420 g of $LiOH \cdot H_2O$ and 1.237 g of H_3BO_3 were used, while 0.246 g of $LiOH \cdot H_2O$ and 0.725 g of H_3BO_3 were used to achieve a thickness of 20 nm. Considering experiment uncertainty, the thicknesses of the deposited LBO layers were estimated as 100 ± 6, 34 ± 3, and 20 ± 2 nm. The estimated thickness error is described in supporting information.

Material characterization

The crystal structure of LCO@LBO powders was determined by powder X-ray diffraction (XRD, Miniflex II equipped with the D/teX Ultra high-speed 1-dimensional detector, Rigaku Ltd., Japan) analysis performed using Cu K_α radiation (λ = 1.54518 Å) in a 2θ range of 10–90° at a sampling width of 0.02 mm, a scan speed of 20.0° min^{-1}, a voltage of 30 kV, and a current of 15 mA. The morphology of LCO@LBO particles was observed by field-emission scanning electron microscopy (FE-SEM; JCM-5700, JEOL Ltd., Japan) at an acceleration voltage of 5 kV. Surface chemical states were investigated by X-ray photoemission spectrometry (XPS; JPS-9200, JEOL Ltd., Japan) using a monochromatic Mg K_α (1253.6 eV) X-ray source at an acceleration tension and intensity of 10 kV and 10 mA, respectively. The pass energy was set to 30 eV, and high-resolution spectra were acquired using a step size of 0.1 eV. In addition, the elemental compositions of the LCO@LBO particle surface and the elemental distributions of particle cross-sections were probed by Auger electron spectroscopy (AES) and scanning Auger microscopy (JAMP-9510F, JEOL Ltd., Japan), respectively. Particles were sectioned by Focused ion beam milling coupled with scanning electron microscopy (FIB-SEM, JIB-4700F Multi Beam System, JEOL Ltd., Japan).

Electrochemistry

The effects of the LBO coating on battery performance were studied using R2032 coin-type half-cells, with bare-LCO half-cells used as controls. Prior to electrode preparation, LCO@LBO and bare LCO were heated at 150 °C in a dry room with a dew point of approximately −40 °C to remove traces of water. The electrode formulation contained the LCO@LBO active material (90 wt%), Denka Black (5 wt%; Denki Chemical Industry Ltd., Japan) and polyvinylidene fluoride (5 wt%; Kishida Chemical Co. Ltd., Japan). The corresponding slurries were prepared using *N*-methyl-2-pyrrolidone (Kishida Chemical Co. Ltd., Japan), cast on Al foil current collectors using a baker-type applicator (PI-1210, Hosen Ltd., Japan), and vacuum-dried at 120 °C (VOM-1000B, Tokyo Rika Kikai Ltd., Japan) overnight. After drying, the cathodes were punched out using a 14-mm hand punch and pressed at 50 kN using a hydraulic press (P-1B, RIKEN KIKI Ltd., Japan). The basis weight of the electrode active material and the electrode density equaled 5.5–6.5 mg and 2.7–2.9 g cm^{-3}, respectively. A 1 M solution of $LiPF_6$ in ethylene carbonate: dimethyl carbonate (EC:DMC, 1:2, v/v) was used as an electrolyte, and polypropylene (Celgard #2400) was used as a separator. Constant current charge-discharge tests were performed using a potentiostat (HJ-SD8 series, Hokuto Denko Ltd., Japan) in a cutoff voltage range of 2.8–4.2 V (*vs.* Li^+/Li). High-rate performance was evaluated at current densities of 0.4, 1, 2, 4, 6, 10, and 16 C. The electrochemical impedance spectra of half-cells were recorded using a potentio-galvanostat (VSP-300, Biologic, France) in the frequency range of 200 kHz to 1.00 mHz for SOCs of 0, 50, and 100% at room temperature and for SOC = 50% at −10, 0, 20, and 40 °C.

Results and discussion

LCO@LBO characterization

Figure 1(a) displays the XRD patterns of bare LCO and LCO@LBO samples, revealing that all peaks matched those of the $LiCoO_2$ reference (ICDD PDF 70-5466), with no modifications of peak shape or position observed. Thus, the deposition of LBO had no influence on the layered rock-salt crystal structure of LCO. Furthermore, no peaks matching those of the LBO reference were detected for LCO@LBO particles irrespective of coating thickness, which indicated that the LBO coating was amorphous. To confirm the stoichiometry of the coating, we independently prepared LBO by heating a precursor solution to 500 °C, revealing that the XRD peaks of the resultant white powder closely matched those of the reference and thus confirming that the LBO layer contained $Li_2B_4O_7$ (Figure 1(b)).

<figure1>

Figure 1. Powder XRD patterns of a) (from top to bottom) bare LCO, LCO@LBO 20 nm, LCO@LBO 34 nm, LCO@LBO 100 nm, $LiCoO_2$ reference (ICDD PDF 70-5466), and $Li_2B_4O_7$ reference (ICDD PDF 18-0717); b) LBO prepared from an aqueous precursor solution and the $Li_2B_4O_7$ reference (ICDD PDF 18-0717). c) FE-SEM images of LCO@LBO 100 nm, LCO@LBO 34 nm, LCO@LBO 20 nm, and bare LCO recorded using backscattered electron detection.

FE-SEM using backscattered electron detection afforded high-contrast images (Figure 1(c)). As these images were constructed from backscattered electrons originating from the sample surface, the bright areas were assigned to the high-electron-density LCO phase, while the dark areas were assigned to the light-element-containing LBO phase. Note that in the case of LCO@LBO 100 nm, the dark phase was clearly present in the intergranular spaces non-homogeneously formed at neighboring LCO particles. The elemental analysis (FE-SEM coupled with Energy dispersive X-ray spectroscopy (EDS)) of LCO@LBO 34 nm clearly identified B and O in the dark areas, implying that these areas primarily contained B_2O_3 presumably formed via phase separation from the LCO@LBO composite (Figure S1).

XPS analysis of LCO@LBO (Figure 2) revealed the presence of low-binding-energy weak satellite peaks (marked as "sat") for almost all orbitals, which was ascribed to the production of minor photoelectric peaks by X-rays non-filtered by the monochromator. No B signals were detected in the B 1s spectra of bare LCO, which allowed for a proper comparison with coated electrodes (Figure 2(a)). In contrast, an intense peak at 192.0 ± 0.4 eV appeared in the high-resolution B 1s spectra of LBO-coated samples. In the case of LCO@LBO 20 nm and LCO@LBO 34 nm, the position of this peak matched that of the $Li_2B_4O_7$ reference (192.3 eV) (Figure 2(b)). Thus, the coordination environment did not significantly depend on crystallinity, i.e., the environment observed for the Li-B-O network formed inside the amorphous LBO layer was similar to that observed for crystalline $Li_2B_4O_7$. In contrast, a broadened peak slightly shifted toward higher binding energies was observed for LCO@LBO 100 nm and could be deconvoluted into two components located at 191.8 eV ($Li_2B_4O_7$) and 193.0 eV (B_2O_3) (Figure 2(c)). These spectral features support our conclusion on the origin of the dark areas in FE-SEM images.

The high-resolution C 1s spectra of LCO@LBO 20 nm and LCO@LBO 34 nm could be deconvoluted into three components centered at 284.6 eV (C–C), 285.3 eV (C–O), and 288.5 eV (O–C=O) (Figure S2(a)) and believed to reflect the presence of surface-adsorbed organic contaminants. Note that the spectrum of LCO@LBO 100 nm featured an additional peak of Li_2CO_3 at 289.7 eV and an elevated relative content of the C–O peak (Figure 2(d)). The formation of Li_2CO_3 was ascribed to the reaction of LiOH (separated from the aqueous precursor solution remaining on the LCO particle surface) with atmospheric CO_2, in line with the results of previous studies.[23] The Li 1s spectra (Figure 2(e)) were characterized by a strong overlap between the Li 1s peaks at 54.0 eV and the satellite peaks of the Mg K_α X-ray source at ~51.8 eV. Moreover, a third (Co 3p–related) peak was observed at high binding energy. As the Li peaks were not fully resolved, the deconvolution of $Li_2B_4O_7$ and $LiCoO_2$ contributions could not be performed with satisfactory precision for coated samples. However, the increased intensity of the Li 1s peaks of LCO@LBO samples suggested that the local concentration of Li on the LCO particle surface was genuinely increased by LBO layer deposition. In addition, high-resolution Co 2p (Figure 2(f)) spectra featured Co $2p_{3/2}$ and Co $2p_{1/2}$ peaks (at 780.0 and 795.1 eV, respectively) with binding energies and shapes characteristic of LCO samples.[24] Thus, the deposition of an amorphous LBO layer did not significantly affect the oxidation state of Co on the LCO particle surface. High-resolution O 1s spectra (Figure S2(b)) featured a narrow peak at 529.4 eV characteristic of oxygen atoms in the LCO crystalline network and two peaks of weakly surface-adsorbed species at 531.1 and 532.2 eV. In this case, again, the LBO coating did not influence the oxide components and was therefore concluded not to affect the initial chemical composition of the LCO surface. Interestingly, Co and oxide components were observed for all LCO@LBO surfaces irrespective of coating thickness. Therefore, the coating layer was assumed to be heterogeneously distributed on LCO particles, which could explain the detection of bare LCO at some points of the sample surface.

<figure2>

Figure 2. High-resolution B 1s spectra of a) bare LCO (black), LCO@LBO 20 nm (green), LCO@LBO 34 nm (blue), and LCO@LBO 100 nm (red); and b) $Li_2B_4O_7$ powder prepared from an aqueous precursor solution as a reference. c) Deconvoluted B 1s spectrum of LCO@LBO 100 nm. d) High-resolution C 1s spectrum of LCO@LBO 100 nm. e) Li 1s and f) Co 2p high-resolution spectra of bare LCO (black), LCO@LBO 20 nm (green), LCO@LBO 34 nm (blue), and LCO@LBO 100 nm (red).

As a technique complementary to XPS surface analysis, AES was used to visualize the spatial distribution of B compounds on the LCO particle surface with high lateral resolution and thus shed light on the morphological characteristics of LCO@LBO particles. AES spectra (Figure S3) and the corresponding chemical mappings (Figure 3) were recorded for FIB-cross-sectioned LCO@LBO particles to obtain better spatial information on thickness uniformity. The mappings obtained for three LCO@LBO samples showed that a large amount of B was distributed along the cross-section contour, i.e., on the particle surface. These results indicated that the LBO coating was probably inhomogeneous in thickness but was well distributed on the LCO particle surface.

<figure3>

Figure 3. a) SEM image and b) AES chemical mapping of the B KLL transition of a FIB-cross-sectioned LCO@LBO 100 nm particle. c) SEM image and d) AES chemical mapping of the B KLL transition of a FIB-cross-sectioned LCO@LBO 34 nm particle. e) SEM image and f) AES chemical mapping of the B KLL transition of a FIB-cross-sectioned LCO@LBO 20 nm particle.

Electrochemical characteristics

The effect of the amorphous LBO layer on the kinetic parameters of LCO electrodes was probed by EIS analysis of half-cells at SOCs of 0, 50, and 100%, with the Nyquist plots (Figure 4(a)-(c)), equivalent circuits (Figure 4(d)-(e)), and Bode diagrams (Figure 4(f)-(h)) used for fitting. Prior to EIS measurements, all half-cells were subjected to three cycles within a cutoff voltage range of 2.8–4.2 V (*vs.* Li$^+$/Li) at a current density of 0.2 C. At a SOC of 0%, two semicircles were observed between 5793 and 200 kHz and between 82 and 5793 Hz (Figure 4(a)). The presence of three resistive components with different time constants was confirmed according to the corresponding Bode diagrams, even though the circular arcs observed in the Nyquist plots at ≤82 Hz were not individually separated (Figure 4(f)). This suggested that the LBO coating increased the impedance response at extremely low frequencies. For half-cells with SOCs of 50 and 100%, two further semicircles were observed in the low-frequency range of 7.9–82 Hz, while another semicircle and linear behavior (assigned to Warburg impedance due to the diffusion of Li$^+$ within the electrodes) were observed below 7.9 Hz. Numerical analysis using equivalent circuit models was performed to identify the contributions of all impedance components. Note that the equivalent circuit used for SOC = 0% (Figure 4(d)) was different from that used for SOC = 50 and 100% (Figure 4(e)). The respective resistance components in descending order according to frequency were R2, R3, R4, and R5 (Table 1). As the low-frequency region of SOC = 0% was difficult to fit as a semicircle, resistance components were assigned to the two high-frequency semicircles, and both resistances were calculated by fitting.

The semicircle located between 5793 and 200 kHz (assignable to R2) was observed at all SOCs irrespective of coating thickness, and the corresponding resistances were small (0.7–2.6 Ω) and unaffected by the SOC and LBO presence. Therefore, R2 was identified as the resistance of the Li metal anode. A semicircle between 82 and 5793 Hz (assignable to R3) was also observed for all samples. R3, reflecting the resistance due to Li$^+$ diffusion within the CEI layer,[25,26] increased as the SOC increased from 0 to 50% and dropped again as the SOC further increased to 100%, which strongly supported our above assumption. As the potential reached 3.9 V at a SOC of 50%, impedance growth was closely related to CEI formation at the cathode surface. In contrast, the subsequent evolution of R3 observed at the end of charging was attributed to CEI dissolution at high potentials (4.2 V), in line with the results obtained for other electrode systems.[27] Interestingly, R3 decreased upon the application of the LBO coating, and the extent of this decrease depended on the coating thickness, e.g., LCO@LBO 100 nm, which had the largest coating thickness, exhibited the lowest R3 at all SOCs. These kinetic characteristics suggested that the LBO coating effectively mitigated the overgrowth to CEI layer formation at the electrolyte interface by limiting contact area of electrolyte and LCO surface. FE-SEM images of bare, LCO@LBO 20nm and LCO@LBO 34nm electrodes after 200 cycles operated at 2C were shown in Figure S4, respectively. Small particles were distinguished on bare surface, clearly, as compared to those of LBO coated LCO electrodes. These small particles might be assignable to the CEI layer via side reactions happened at the interface. These CEI layer-based particles are less present on LCO@LBO 20 nm and barely visible on LCO@LBO 34 nm. Furthermore, since overall the morphology of the LCO@LBO particles is seemed to be maintained without seen any crack formation, suggesting that the LBO coating layer will be stably existing without any obvious degradation upon cycling. Therefore, even if the LBO layer is not evenly distributed over the entire surface of the LCO particles, it is considered that the physical barrier effect contributes to the suppression of excessive oxidative decomposition of the electrolyte solution due to side reactions.[28]

Two additional semicircles corresponding to R4 and R5 were observed at low frequencies in Nyquist plots, as suggested by the corresponding Bode plots (Figure 4(f)–(h)). The semicircle assigned to R4 was observed at 7.9–82 Hz and was believed to represent charge transfer reaction–related resistance.[13,14] As the application of the LBO coating (irrespective of its thickness) decreased R4 relative to the value observed for bare LCO, the LBO layer was considered to accelerate Li$^+$ transfer processes such as the desolvation of Li$^+$ solvated by the electrolyte solvent, the adsorption and subsequent surface diffusion of desolvated Li$^+$ on the active material surface through the CEI layer, and the subsequent insertion of Li$^+$ into LCO. As reported in literature, the semicircles between 0.1 and 10 Hz reflected the resistance due to Li$^+$ insertion into the active material lattice.[26] The resistance due to the insertion reaction could be represented by the impedance component (R5) related to the semicircle at ≤7.9 Hz. Indeed, any significant difference to the irrespective of the SOC or LBO thickness did not be given from R5 resistance values observation, which suggested that for the insertion process, the LBO coating had no influence on Li$^+$ diffusion resistance. Therefore, the intercalation reaction did not contribute to the evolution of R4 driven by the deposition of the LBO coating. The effect of the local concentration of Li$^+$

at the extreme surface of LBO-coated LCO particles was proposed as a plausible and new method of kinetic parameter control in interfacial Li^+ transportation, which suggested that the application of the LBO coating changed the rate-determining step from the desolvation process of Li^+ solvated by the electrolyte solvent to surface Li^+ exchange reaction (Li^+ adsorption and diffusion processes). The capacitive components contributing to each impedance (evaluated using equivalent circuits) are summarized in Table 1. The increase in capacitive component with increasing film thickness implied that the presence of LBO layer locally increased the Li^+ concentration at LCO particles surface in the composite electrodes. LCO@LBO 20 nm and LCO@LBO 34 nm showed lower R4 than LCO@LBO 100 nm, which suggested that the promotional effect of the LBO coating on Li^+ exchange slightly decreased when the coating thickness exceeded a certain value. Specifically, an excessively thick layer of the insulating LBO was believed to block the electron conduction path. Furthermore, the effect of higher resistive layer formation at the LCO\LBO interface due to space charge layer becomes non-negligible as the increase of LBO thickness. These results suggested the existence of a trade-off between the acceleration of Li^+ exchange reaction kinetics driven by local increase in Li^+ concentration and the impedance growth based on the suppression of electron conduction as well as based on space charge effect by the LBO coating.

<Figure 4>

Figure 4. Results of EIS measurements performed for variable-SOC half-cells after three cycles at 0.2 C and room temperature. Nyquist plots obtained for SOCs of a) 0, b) 50, and c) 100%. Equivalent circuits used to fit the behavior of cells with SOCs of d) 0 and e) 50 and 100%. Bode diagrams of cells with SOCs of f) 0, g) 50, and h) 100%.

Table 1. Impedance parameters for cells with various SOCs.

<Table 1>

LCO@LBO 20 nm half-cells with a SOC of 50% were further probed by EIS at −10, 0, 20, and 40 °C to determine activation energies and thus deeper understand the above frequency-based assignment of impedance components. The corresponding Arrhenius plots and activation energies (calculated using the method of Nakayama *et al.*[29]) are given in Figure 5(c) and (d). A linear change with temperature was observed for all resistance components. It is indicating that each resistance components were successfully separated into single component having different time constant. As R2 was not significantly affected by temperature, it was concluded to originate from the Li metal anode. The activation energy calculated from R3 data (0.68 eV) agreed with that reported for Li^+ diffusion in the LBO glass matrix (0.70 eV).[30] Therefore, R3 was concluded to predominantly originate from the LBO coating deposited on LCO particles. However, the value of 0.68 eV exceeded the previously reported activation energy of 0.39 eV, which was attributed to Li^+ diffusion in the electrochemically formed CEI layer on the cathode surface.[31] We think that the contributions of LBO and CEI layers can hardly be separated because of their similar time constants.

The activation energy of charge transfer in LCO@LBO 20 nm electrodes (0.40 eV) was lower than those reported for the solvation of Li^+ by open-chain carbonates (typically 0.50–0.70 eV).[30,32,33] This suggested that LBO coating deposition is accompanied by a decrease in activation energy and thus accelerates the sluggish desolvation reaction in the electric double layer formed at the electrode interface, which is generally assumed to be the rate-determining step (Figure 5(e)). Finally, the activation energy corresponding to R5 coincided with that reported for the insertion of Li^+ into the active material lattice.[26] Hence, the LBO coating did not remarkably modify the mechanism of Li^+ insertion into the LCO lattice.

The LBO coating locally increased the concentration of Li^+ near the LCO particle surface compared to that of bare LCO particles surrounded by solvated Li^+ dispersed in the liquid electrolyte. Thus, the above findings suggest the enhancement of local Li^+ concentration via solid electrolyte coating reduce an activation energy of the desolvation process more than the Li^+ adsorption and diffusion process, as explained in Figure 5(e). We emphasize that all environmental changes driven by the LBO coating contribute to C-rate capability enhancement in the discharge process accompanied by Li^+ intercalation into the LCO lattice.

<Figure 5>

Figure 5. a, b) Nyquist plots of LCO@LBO 20 nm with a SOC of 50% recorded at −10, 0, 20, and 40 °C; c) plot of $\ln(1/R)$ *vs.* $1/T$ for different resistances; d) equivalent circuit used for fitting and table of calculated activation energies related to each R; e) schematic illustration of the influence of the LBO coating on the reaction diagram of Li^+ insertion.

Figure 6(a) shows galvanostatic discharge profiles of half-cells at various C-rates, with all charge processes performed under controlled conditions in the constant current constant voltage (cccv) mode at a constant C-rate. Notably, the LBO coating did not significantly change the reaction mechanism, including phase stability depending on Li composition and the overpotential for the redox reaction. The sharp voltage drop observed around 4.1 V was closely related to the hexagonal-to-monoclinic phase transition,[34] while the subsequent gradual change in voltage slope observed around 3.9 V was due to the solid-solution reaction. Compared to that observed at 0.4 C, the working voltage for the solid-solution redox reaction of $Co^{4+} \rightarrow Co^{3+}$ decreased at higher discharge C-rates in all cells, which was ascribed to the growth of internal resistance with increasing current density. Note that the voltage drop was attenuated in comparison with that of the bare LCO electrodes, which confirmed that the LBO layer mitigated the growth of internal resistance with increasing current density. As shown in Figure 6(b), capacity retention at 10 C was higher for half-cells based on LBO-coated electrodes. Furthermore, the effect of LBO coating on capacity retention was probed at a current density of 16 C. As a result, the LCO@LBO 20 nm electrode exhibited the highest capacity retention of ~79%, which indicated that the LBO coating clearly contributed to C-rate capability enhancement in the discharge process and that the kinetic features of galvanostatic charge-discharge tests were in good agreement with the trends observed for EIS experiments. An excessively thick LBO layer was further found to decrease performance.

Cyclic voltammetry (CV) was further performed to determine the effect of amorphous LBO layer coating on the electrochemical polarization and kinetics. We compared the kinetics during lithiation/delithiation reactions in the half-cells (Figure S5). The LCO@LBO electrodes showed a broad peak envelope at ~3.6V during the cathodic scan clearly consists of at least two peaks, one at 3.7-3.85V (depending on the scan rates) and another on at around 3.45V. Note that the peak at 3.45V is only observed in the LCO@LBO electrode (not in the pure LCO electrode) and it only emerges at a relatively high scan rate (>0.6mV/s). These all results are indicating that there is an additional Faradaic Li-ion storage process in the LCO@LBO samples at ~3.45V and this process might be strongly related to be diffusion-limited reaction. In contrast, the LCO-bare electrode represented a broader and lower redox peak at a slow sweep rate, as comparing to those of the LCO@LBO electrodes. Thus, it is indicating that Li+ diffusion rate becomes faster at around the LCO particle surface by LBO coating. This might be the effect of increase of the Li+ concentration on the surface. The all results demonstrated in the CV measurements are in good agreement with the battery performance and explain the improved C-rate capability.

As solid electrolytes generally show a lower dependence of Li^+ conductivity on temperature than non-aqueous liquid electrolytes, we further performed C-rate capability tests at −10 °C to understand the kinetic limitations of the LBO coating (Figure 6(c) and (d)). The discharge curves recorded at 0.4 C showed features similar to those observed at room temperature. In contrast, the working voltages significantly decreased with increasing current density, which suggests that the growth of internal resistance due to the Li^+ diffusion limit to electrode surface from the bulk electrolyte with increasing current density was becoming tangible at low temperature. Notably, the LCO@LBO 34nm coating could still sufficiently mitigate capacity degradation at rates of up to 10 C even at low temperature with a capacity retention of 45% of the initial value against 18% for the reference material, and the decreased charge transfer resistance of the LBO-coated electrode was most pronounced at low temperatures. The impacts of LBO coating completely vanished when the test was performed at 16 C, which indicated that the effect of the LBO film reached its limit under these conditions and suggested that the rate-determining step again shifted from Li^+ exchange or desolvation at the electrode interface to Li^+ mass transfer in the electrolyte.

<figure6>

Figure 6. a) Discharge curves recorded at 0.4, 6, and 16 C for bare LCO, LCO@LBO 20 nm, LCO@LBO 34 nm, and LCO@LBO 100 nm electrodes at room temperature; b) effects of cycling on the specific discharge capacities at 0.4, 1, 2, 4, 6, 10, and 16 C for the above electrodes at room temperature; c) discharge curves of the above electrodes recorded at −10 °C; d) effects of cycling on specific discharge capacities of the above electrodes determined at various C-rates at −10 °C.

Conclusions

Surface chemical state analysis and electrochemical analysis using coin-type half-cells were used to demonstrate the effects of coating LCO particles with amorphous LBO on the properties of the corresponding electrodes, especially from the perspective of kinetics. EIS analysis of LCO@LBO electrodes at designated SOCs revealed that the LBO layer accelerates charge transfer, which is typically limited by the desolvation of Li^+ solvated by open-chain carbonates at the electrolyte interface. Furthermore, the calculated activation energies strongly suggested that Li^+ transfer within the LBO (0.40 eV) required less energy than the desolvation mechanism (0.50–0.70 eV) that would occur on the bare cathode material. The diffusion-controlled step accompanied by desolvation is widely accepted to be the rate-determining process in battery reactions; however, our results revealed that the LBO solid electrolyte coating increased the local Li^+ concentration on the LCO particle surface to shift the rate-determining step to the reaction-controlled process. Thus, this is the first report providing a full picture of the effects of coating the surface of cathode active material particles with a solid electrolyte and showing that the use of solid electrolyte coatings is a promising new direction for the development of high-power LIB cathode materials.

Conflicts of interest

There are no conflicts to declare.

Acknowledgements

This work was partially supported by JSPS KAKENHI (17H01322), MEXT Regional Innovation Strategy Support Program and JST OPERA.

Notes and references

1 A. Wang, S. Kadam, H. Li, S. Shi and Y. Qi, *npj Comput. Mater.*, 2018, 4, 1–26.

2 T. Abe, H. Fukuda, Y. Iriyama and Z. Ogumi, *J. Electrochem. Soc.*, 2004, **151**, A1120.

3 T. Abe, F. Sagane, M. Ohtsuka, Y. Iriyama and Z. Ogumi, *J. Electrochem. Soc.*, 2005, **152**, A2151.

4 T. R. Jow, S. A. Delp, J. L. Allen, J.-P. Jones and M. C. Smart, *J. Electrochem. Soc.*, 2018, **165**, A361–A367.

5 X. Li, J. Liu, M. N. Banis, A. Lushington, R. Li, M. Cai and X. Sun, *Energy Environ. Sci.*, 2014, **7**, 768–778.

6 D. Jin, D. Song, A. Friesen, Y. M. Lee and M. H. Ryou, *Electrochim. Acta*, 2018, **259**, 578–586.

7 Y. Zhai, W. Yang, D. Ning, J. Yang, L. Sun, G. Schuck, G. Schumacher and X. Liu, *J. Mater. Chem. A*, 2020, **8**, 5234–5245.

8 J. Lu, Q. Peng, W. Wang, C. Nan, L. Li and Y. Li, *J. Am. Chem. Soc.*, 2013, **135**, 1649–1652.

9 J. Cao, H. Xie, F. Lv, N. Xu, W. S. V. Lee, Y. Ma, Y. Liu, Z. Cheng and L. Chen, *ACS Appl. Energy Mater.*, 2020, **3**, 5462–5471.

10 L. L. Zhang, J. Q. Wang, X. L. Yang, G. Liang, T. Li, P. L. Yu and D. Ma, *ACS Appl. Mater. Interfaces*, 2018, **10**, 11663–11670.

11 J. Zhang, J. Zhang, X. Ou, C. Wang, C. Peng and B. Zhang, *ACS Appl. Mater. Interfaces*, 2019, **11**, 15507–15516.

12 Z. Wang, H. Zhong and G. Song, *J. Alloys Compd.*, 2020, **849**, 156467.

13 Z. Xiao, Z. Chi, L. Song, Z. Cao and A. Li, *Ceram. Int.*, 2020, **46**, 8328–8333.

14 J. Duan, C. Wu, Y. Cao, K. Du, Z. Peng and G. Hu, *Electrochim. Acta*, 2016, **221**, 14–22.

15 J. Zhu, Y. Li, L. Xue, Y. Chen, T. Lei, S. Deng and G. Cao, *J. Alloys Compd.*, 2019, **773**, 112–120.

16 B. Huang, X. Yang, G. Xu, M. Wang and Y. Gu, *Ionics (Kiel).*, 2019, **25**, 5819–5827.

17 D. Wohlmuth, V. Epp, B. Stanje, A. M. Welsch, H. Behrens and M. Wilkening, *J. Am. Ceram. Soc.*, 2016, **99**, 1687–1693.

18 Y. Kato, S. Hori, T. Saito, K. Suzuki, M. Hirayama, A. Mitsui, M. Yonemura, H. Iba and R. Kanno, *Nat. Energy*, 2016, **1**, 1–7.

19 S. Boulineau, M. Courty, J. M. Tarascon and V. Viallet, *Solid State Ionics*, 2012, **221**, 1–5.

20 H. Tsukasaki, S. Mori, H. Morimoto, A. Hayashi and M. Tatsumisago, *Sci. Rep.*, 2017, **7**, 1–7.

21 S. Ohta, T. Kobayashi and T. Asaoka, *J. Power Sources*, 2011, **196**, 3342–3345.

22 K. Ohara, A. Mitsui, M. Mori, Y. Onodera, S. Shiotani, Y. Koyama, Y. Orikasa, M. Murakami, K. Shimoda, K. Mori, T. Fukunaga, H. Arai, Y. Uchimoto and Z. Ogumi, *Sci. Rep.*, 2016, **6**, 1–9.

23 Z. Chen and J. R. Dahn, *Electrochem. Solid-State Lett.*, 2004, **7**, A11–A14.

24 L. Dahéron, H. Martinez, R. Dedryvère, I. Baraille, M. Ménétrier, C. Denage, C. Delmas and D. Gonbeau, *J. Phys. Chem. C*, 2009, **113**, 5843–5852.

25 D. D. Liang, H. F. Xiang, X. Liang, S. Cheng and C. H. Chen, *RSC Adv.*, 2017, **7**, 6809–6817.

26 M. Nakayama, H. Taki, T. Nakamura, S. Tokuda, R. Jalem and T. Kasuga, *J. Phys. Chem. C*, 2014, **118**, 27245–27251.

27 Y. Charles-Blin, D. Flahaut, J.-B. Ledeuil, K. Guérin, M. Dubois, N. Louvain, L. Monconduit and H. Martinez, *J. Electrochem. Soc.*, 2019, **166**, A1905–A1914.

28 A. M. Wise, C. Ban, J. N. Weker, S. Misra, A. S. Cavanagh, Z. Wu, Z. Li, M. S. Whittingham, K. Xu, S. M. George and M. F. Toney, *Chem. Mater.*, 2015, **27**, 6146–6154.

29 M. Nakayama, H. Ikuta, Y. Uchimoto and M. Wakihara, *J. Phys. Chem. B*, 2003, **107**, 10603–10607.

30 J. H. Cho, G. W. Lee and Y. S. Yang, *Ferroelectrics*, 1997, **196**, 121–124.

31 X. Y. Qiu, Q. C. Zhuang, Q. Q. Zhang, R. Cao, P. Z. Ying, Y. H. Qiang and S. G. Sun, *Phys. Chem. Chem. Phys.*, 2012, **14**, 2617–2630.

32 K. Xu, A. Von Cresce and U. Lee, *Langmuir*, 2010, **26**, 11538–11543.

33 Z. Ogumi, T. Abe, T. Fukutsuka, S. Yamate and Y. Iriyama, in *Journal of Power Sources*, Elsevier, 2004, vol. 127, pp. 72–75.

34 J. Cho, Y. J. Kim and B. Park, *J. Electrochem. Soc.*, 2001, **148**, A1110.

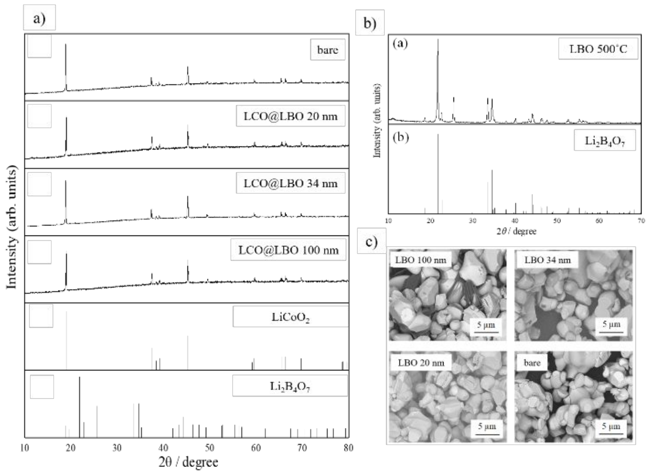

Figure 1. Powder XRD patterns of a) (from top to bottom) bare LCO, LCO@LBO 20 nm, LCO@LBO 34 nm, LCO@LBO 100 nm, LiCoO$_2$ reference (ICDD PDF 70-5466), and Li$_2$B$_4$O$_7$ reference (ICDD PDF 18-0717); b) LBO prepared from an aqueous precursor solution and the Li$_2$B$_4$O$_7$ reference (ICDD PDF 18-0717). c) FE-SEM images of LCO@LBO 100 nm, LCO@LBO 34 nm, LCO@LBO 20 nm, and bare LCO recorded using backscattered electron detection.

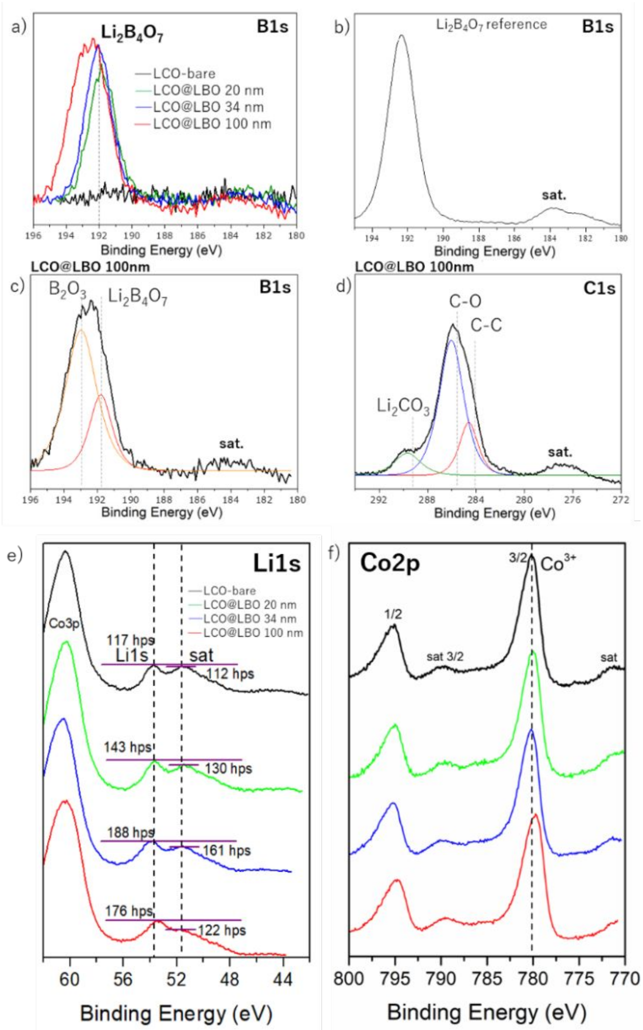

Figure 2. High-resolution B 1s spectra of a) bare LCO (black), LCO@LBO 20 nm (green), LCO@LBO 34 nm (blue), and LCO@LBO 100 nm (red); and b) $Li_2B_4O_7$ powder prepared from an aqueous precursor solution as a reference. c) Deconvoluted B 1s spectrum of LCO@LBO 100 nm. d) High-resolution C 1s spectrum of LCO@LBO 100 nm. e) Li 1s and f) Co 2p high-resolution spectra of bare LCO (black), LCO@LBO 20 nm (green), LCO@LBO 34 nm (blue), and LCO@LBO 100 nm (red).

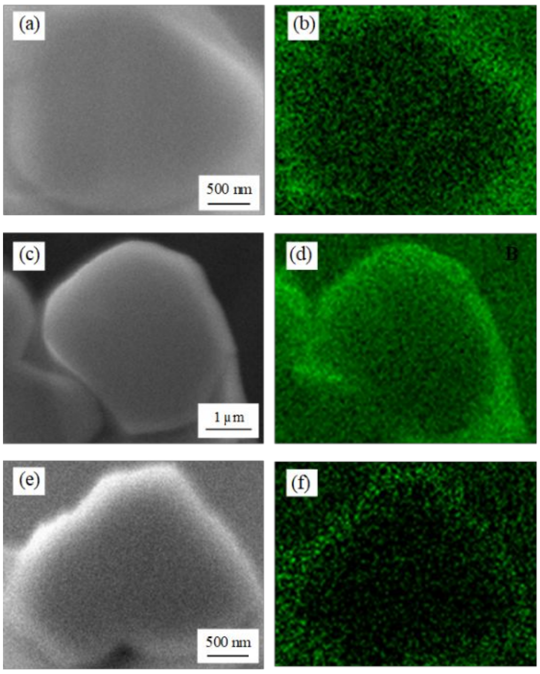

Figure 3. a) SEM image and b) AES chemical mapping of the B KLL transition of a FIB-cross-sectioned LCO@LBO 100 nm particle. c) SEM image and d) AES chemical mapping of the B KLL transition of a FIB-cross-sectioned LCO@LBO 34 nm particle. e) SEM image and f) AES chemical mapping of the B KLL transition of a FIB-cross-sectioned LCO@LBO 20 nm particle.

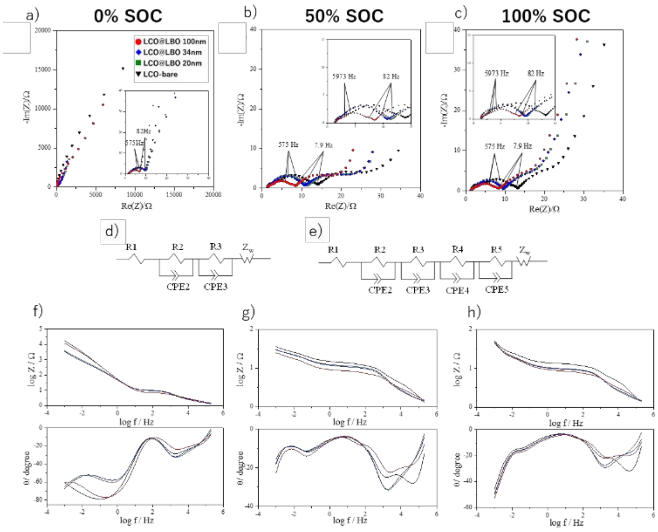

Figure 4. Results of EIS measurements performed for variable-SOC half-cells after three cycles at 0.2 C and room temperature. Nyquist plots obtained for SOCs of a) 0, b) 50, and c) 100%. Equivalent circuits used to fit the behavior of cells with SOCs of d) 0 and e) 50 and 100%. Bode diagrams (top: the relation between impedance magnitude and frequency, bottom: the relation between impedance phase and frequency) of cells with SOCs of f) 0, g) 50, and h) 100%.

Table 1. Impedance parameters for cells with various SOCs.

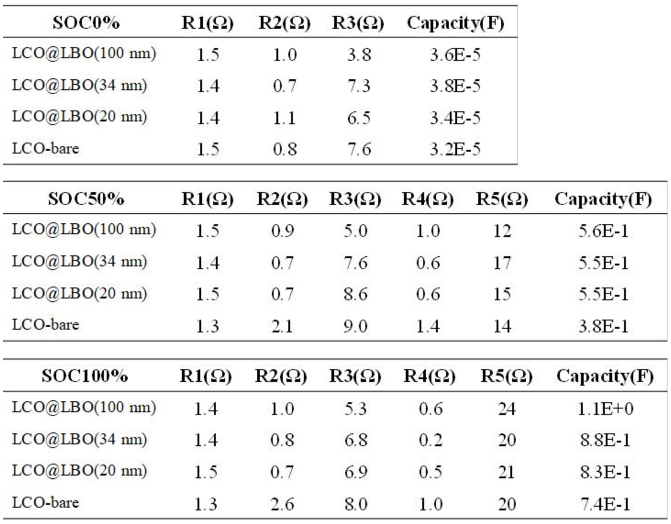

SOC0%	R1(Ω)	R2(Ω)	R3(Ω)	Capacity(F)
LCO@LBO(100 nm)	1.5	1.0	3.8	3.6E-5
LCO@LBO(34 nm)	1.4	0.7	7.3	3.8E-5
LCO@LBO(20 nm)	1.4	1.1	6.5	3.4E-5
LCO-bare	1.5	0.8	7.6	3.2E-5

SOC50%	R1(Ω)	R2(Ω)	R3(Ω)	R4(Ω)	R5(Ω)	Capacity(F)
LCO@LBO(100 nm)	1.5	0.9	5.0	1.0	12	5.6E-1
LCO@LBO(34 nm)	1.4	0.7	7.6	0.6	17	5.5E-1
LCO@LBO(20 nm)	1.5	0.7	8.6	0.6	15	5.5E-1
LCO-bare	1.3	2.1	9.0	1.4	14	3.8E-1

SOC100%	R1(Ω)	R2(Ω)	R3(Ω)	R4(Ω)	R5(Ω)	Capacity(F)
LCO@LBO(100 nm)	1.4	1.0	5.3	0.6	24	1.1E+0
LCO@LBO(34 nm)	1.4	0.8	6.8	0.2	20	8.8E-1
LCO@LBO(20 nm)	1.5	0.7	6.9	0.5	21	8.3E-1
LCO-bare	1.3	2.6	8.0	1.0	20	7.4E-1

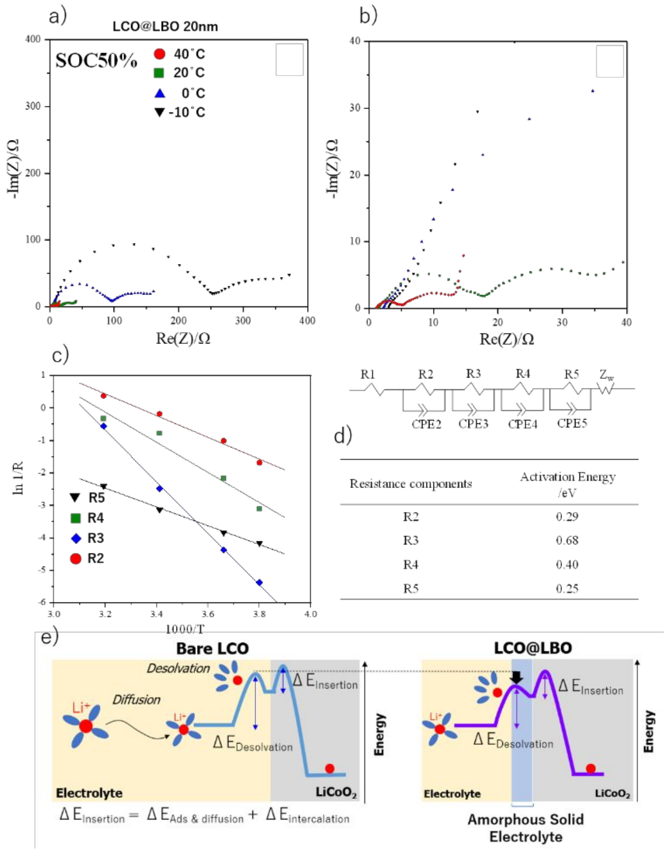

Resistance components	Activation Energy /eV
R2	0.29
R3	0.68
R4	0.40
R5	0.25

Figure 5. a, b) Nyquist plots of LCO@LBO 20 nm with a SOC of 50% recorded at −10, 0, 20, and 40 °C; c) plot of ln(1/*R*) *vs.* 1/*T* for different resistances; d) equivalent circuit used for fitting and table of calculated activation energies related to each R; e) schematic illustration of the influence of the LBO coating on the reaction diagram of Li$^+$ insertion.

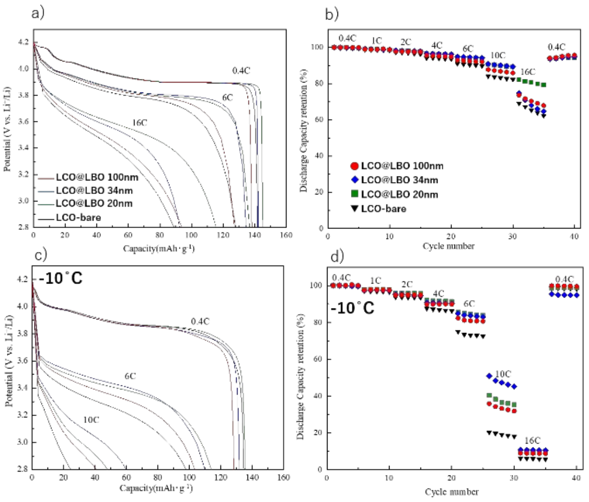

Figure 6. a) Discharge curves recorded at 0.4, 6, and 16 C for bare LCO, LCO@LBO 20 nm, LCO@LBO 34 nm, and LCO@LBO 100 nm electrodes at room temperature; b) effects of cycling on the specific discharge capacities at 0.4, 1, 2, 4, 6, 10, and 16 C for the above electrodes at room temperature; c) discharge curves of the above electrodes recorded at −10 °C; d) effects of cycling on specific discharge capacities of the above electrodes determined at various C-rates at −10 °C.